Contents lists available at ScienceDirect

Applied Catalysis B: Environmental

Research Paper

p-AgI anchored on {001} facets of n-Bi$_2$O$_2$CO$_3$ sheets with enhanced photocatalytic activity and stability

Lili Zhang[a], Chun Hu[a,b,*], Huanhuan Ji[a,b]

[a] Key Laboratory of Drinking Water Science and Technology, Research Center for Eco-Environmental Sciences, Chinese Academy of Sciences, Beijing 100085, China
[b] University of Chinese Academy of Sciences, Beijing 100049, China

ARTICLE INFO

ABSTRACT

A close-connected p-AgI/n-Bi$_2$O$_2$CO$_3$ heterojunction was synthesized by a one-step co-crystallization method. The visible-light-driven photoactivity of AgI was exceptionally enhanced by nearly 5 times through in-situ close contact with Bi$_2$O$_2$CO$_3$. After seven cycling measurements, the photodegradation rate of 2-chlorophenol could be maintained at 88% and no Ag$^+$ and Bi^{3+} could be detected in the reaction solution, indicating high photostability of the heterojunction photocatalyst. On the basis of the characterization of morphology, X-ray diffraction, Fourier-transform infrared spectra and X-ray photoelectron spectroscopy, AgI nanoparticles were selectively anchored on active {001} facets of layered Bi$_2$O$_2$CO$_3$ sheets, and a strong interfacial interaction between p-AgI and n-Bi$_2$O$_2$CO$_3$ was observed, which enhanced effective separation and transfer of the photo-generated electron-hole pair from AgI, resulting in the high photoactivity and photostability of AgI for the degradation and mineralization of 2-chlorophenol under visible light. By the studies of electron spin resonance and other experiments, the charge transfer process at the interface of p-AgI/n-Bi$_2$O$_2$CO$_3$ was verified that the photoexcited electrons of the conduction band of AgI transferred to the conduction band of Bi$_2$O$_2$CO$_3$ to react with surface adsorbed oxygen into O$_2^{\bullet-}$, while the photoexcited holes of the valence band of AgI could oxidize organic pollutants in water.

1. Introduction

Semiconductor photocatalysis has been paid immense attention for its potential applications in solving environmental pollution and energy shortage problems [1–4]. Semiconductors with a wide-band gap usually possess strong reduction and oxidation power and charge separation efficiency, whereas they suffer from low efficiency in utilizing the full solar spectrum. A narrow-band gap semiconductor can efficiently absorb visible light, but it is subjected to the ineffective charge separation and the recombination of the photogenerated carriers. For an optimized use of solar energy, the development of efficient and stable visible-light-active photocatalysts is required. To produce photocatalysts responsive to visible light, some efforts have been recently made, including doping of nonmetals (C, N, S, etc.) [5], deposition of noble metals (Ag, Au, Pt, etc.) [3], and formation of heterostructures between wide-band gap and narrow-band gap semiconductors [6]. Most recently, enhanced visible-light-responsive photocatalytic activity has been realized over BiOCl/Bi$_2$O$_3$ [7], AgBr/BiOBr [8], AgI/BiOI [9], BiOI/BiOIO$_3$ [10], and Ag$_2$O/Bi$_2$O$_2$CO$_3$ [11] hybrid p-n heterojunction photocatalysts. In fact, an effective p-n heterojunction should have the matched band structure, requisite bandgap energy, and close contact between the hybrid semiconductors [8]. It has been proved that the one-step method of fabricating p-n heterojunctions is more superior than the construction method by compositing the individual components [8–10], due to the enabled intimate interfacial interaction for efficiently promoting the charge transfer. Therefore, it is necessary to develop an in-situ convenient way to prepare the effective p-n heterojunction photocatalysts.

In recent years, bismuth-based nanostructured materials have received great attention as potential candidates for highly active photocatalysts. As a kind of n-type semiconductors, bismuth subcarbonate (Bi$_2$O$_2$CO$_3$) has the interesting "Sillén" or "Aurivillius" related structure with alternating Bi$_2$O$_2^{2+}$ and CO$_3^{2-}$ layers [12]. The layered structure inherent in Bi$_2$O$_2$CO$_3$ enables it with a large internal electric field and asymmetrical polarization effect, enhancing the charge separation efficiency. It was disclosed that Bi$_2$O$_2$CO$_3$ single-crystal lamellas with exposed {001} facets enable more effi-

* Corresponding author at: Key Laboratory of Drinking Water Science and Technology, Research Center for Eco-Environmental Sciences, Chinese Academy of Sciences, Beijing 100085, China.
E-mail address: huchun@rcees.ac.cn (C. Hu).

cient charge separation [12]. Moreover, $Bi_2O_2CO_3$ can provide large specific surface area which determined the photocatalytic activity of semiconductors to some extent [13]. However, the relatively large band gap (about 3.3 eV) of pristine $Bi_2O_2CO_3$ limited its application to photodegradation under visible light. In order to enhance adsorption of visible light, a number of strategies have been developed, such as metal (Ag, Bi, etc.) [13,14] or nonmetal (CO_3^{2-}, N, etc.) doping to narrow the band gap [4,15], coupling with other semiconductors including Bi_2MoO_6 [16], BiOI [17], Bi_2S_3 [18], Ag_2O [11] and so on. On the other hand, silver halides (AgX) are well-known photosensitive materials and source materials in photographic films. As a member of AgX, AgI possesses strong visible light absorption ability due to its narrow band gap (about 2.8 eV) [19]. Nevertheless, in most cases the newly deposited AgI phases are micron-sized agglomerates and lack close connection with the original supports, thereby leading to the increased recombination of the photogenerated carriers [20]. Therefore, it is important to design rational approaches to synthesize AgI with good dispersion and smaller sizes, endowing the hybrids with enhanced activity and stability.

Herein, we report *p*-AgI nanoparticles dispersedly anchored on {001} facets of layered *n*-$Bi_2O_2CO_3$ sheets fabricated with a one-step co-crystallization method. The properties of the *p*-AgI/*n*-$Bi_2O_2CO_3$ composite photocatalyst such as morphology, crystal structure, optical property, matched band-edges, electrochemical characteristics, and photocatalytic activity were systematically characterized and evaluated, and the mechanism of the enhanced photocatalytic activity and photostability was proposed.

2. Experimental

2.1. Materials synthesis

$AgI/Bi_2O_2CO_3$ was synthesized using a one-step co-crystallization method. In a typical procedure, $AgNO_3$ (0.21 g) in NH_4OH (2.3 mL, 25% wt% NH_3) was added in 200 mL of ultrapure water and sonicated for 30 min. 6.2 mL of KI aqueous solution (0.2 M) was then slowly added to the above solution and stirred for 30 min. Next, 0.239 g $Bi(NO_3)_3 \cdot 5H_2O$ dissolved in dilute acetic solution was dropwise added to the suspension. The mixture was then stirred in dark for 12 h. The product was filtered, washed, and dried at 70 °C. In addition, the content of bismuth in the sample was determined by inductively coupled plasma optical emission spectrometry (ICP-OES, Optima 2000) after the sample was dissolved using nitric acid overnight, and thus the real loading amount of AgI was obtained to be 70 wt%. Following this procedure, various catalysts were prepared with AgI contents of 48 wt%, 70 wt% and 82 wt%, and the catalyst with 70 wt% AgI exhibited the highest photoactivity (Fig. S1). The catalyst $AgI/Bi_2O_2CO_3$ with 70 wt% AgI was used for all of the subsequent experiments unless otherwise specified. For comparison, AgI and $Bi_2O_2CO_3$ were separately prepared as described above without $Bi(NO_3)_3 \cdot 5H_2O$ or $AgNO_3$ and KI added.

2.2. Materials characterization

Morphological studies were carried out using a field emission scanning electron microscope (FESEM, Hitachi, SU8020). The high resolution transmission electron microscopy (HRTEM) images of the samples were obtained using a JEOL-2010 TEM with an acceleration voltage of 200 kV. The Brunauer-Emmett-Teller (BET) surface area of various samples was determined by nitrogen adsorption/desorption experiments using a surface area and porosity analyzer (ASAP 2020 HD88). Powder X-ray diffraction (XRD) patterns were recorded using a Scintag-XDS-2000 diffractometer with Cu Kα radiation (λ = 1.540598 Å). X-ray photoelectron spectroscopy

(XPS) data were measured via an AXIS-Ultra instrument from Kratos using monochromatic Al Kα radiation (225 W, 15 mA, 15 kV) and low-energy electron flooding for charge compensation. To compensate for surface charge effects, binding energies were calibrated using the C1s hydrocarbon peak at 284.8 eV. UV–vis diffuse reflectance spectra were collected on a Shimadzu U3900 recording spectrophotometer equipped with an integrating sphere. ESR spectra were obtained using a Bruker model ESP 300E electron paramagnetic resonance spectrometer.

Photoelectrochemical measurements were mainly performed using a conventional three-electrode cell system and a CHI 660D electrochemical workstation. The photocatalyst electrode was employed as the working electrode, and a platinum electrode and a saturated calomel electrode served as the counter and reference electrodes, respectively. The electrochemical impedance spectroscopy (EIS) was operated in the frequency range of $0.1–10^5$ Hz in 0.1 M Na_2SO_4 solution. Mott-Schottky analysis was measured in a basic electrochemical system (AMETEK Princeton Applied Research, Oak Ridge, TN) with a two-compartment, three-electrode electrochemical cell. The reference electrode was a Ag/AgCl electrode.

2.3. Photocatalytic activity measurements

The photocatalytic activities of the samples were evaluated by the degradation of 2-chlorophenol (2-CP) under 150 W Xe arc lamp with a 400 nm cutoff filter at room temperature and neutral pH. The incident visible light intensity was 3.5 mW cm^{-2}, which was measured with a radiometer (Photoelectric Instrument Factory Beijing Normal University). 0.1 g photocatalysts were dispersed in 60 mL 2-CP (10 mg L^{-1}) solution with constant stirring. Prior to irradiation, the suspensions were stirred in the dark for 30 min to ensure adsorption-desorption equilibrium. At given time intervals, part of the suspension sample was withdrawn and filtered to remove powders for analysis. The concentration of 2-CP was measured using high-performance liquid chromatography (1200 series; Agilent) with a Zorbax SB-Aq column (5 μm, 4.6 × 250 mm; Agilent). The analysis was carried out at 275 nm using a 60/40% v/v mixture of methol/ultrapure water as mobile phase. The total organic carbon (TOC) of the solution was analyzed using a TOC-V$_{CPH}$ analyzer (Shimadzu). The concentration of chloridion released during the degradation process were monitored by a Dionex model ICS 2000 ion chromatography (IC) equipped with an IonPac AS11-HC analytical column (4 × 250 mm) and using 40 mM KOH as an eluent.

In addition, the possible cation leaching (Ag, Bi) was monitored by ICP-OES on an Optima 2000 (PerkinElmer, Inc.) instrument. To test the stability and recyclability of $AgI/Bi_2O_2CO_3$, the catalyst was filtered, washed with water, and dried at 70 °C. The catalyst was continued to be used in the second cycle. This process was repeated several times.

All of the above experiments were repeated in triplicate and data represented the average of the triplicates with a standard deviation of less than 5%.

3. Results and discussion

3.1. Characterization of photocatalysts

The FESEM micrographs of $Bi_2O_2CO_3$, AgI and $AgI/Bi_2O_2CO_3$ were shown in Fig. 1. AgI consisted of large scale plate-like morphologies with parallel arrangement in different width and thickness. $Bi_2O_2CO_3$ was composed of a large amount of thin sheets due to its internal layered crystal structure with weak van der Waals interactions along the [001] direction [21]. After the in-situ combination of AgI and $Bi_2O_2CO_3$, the morphology of $AgI/Bi_2O_2CO_3$
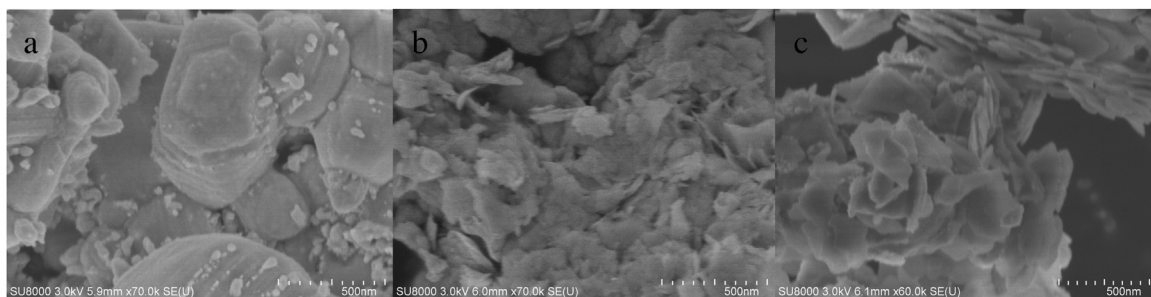
Fig. 1. FESEM images of different samples: (a) AgI, (b) $Bi_2O_2CO_3$, and (c) AgI/$Bi_2O_2CO_3$.
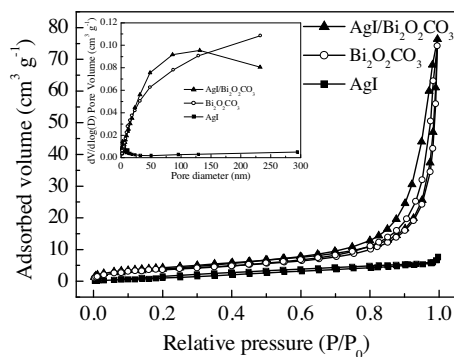
Fig. 2. N_2 adsorption/desorption isotherms of different samples.

Fig. 3. XRD patterns of (a) $Bi_2O_2CO_3$, (b) AgI/$Bi_2O_2CO_3$, (c) AgI, and the standard card of $Bi_2O_2CO_3$ (JCPDS 41-1488). The symbol in (b): (♦) $Bi_2O_2CO_3$, (▼) AgI.

transformed to flower-like architecture composed from dozens of nanoplates and many interstitial spaces between the plate-like particles can be observed. This morphology was expected to enhance light harvest due to multiple scattering and reflection [4]. The N_2 adsorption/desorption isotherms of the AgI, $Bi_2O_2CO_3$ and AgI/$Bi_2O_2CO_3$ samples were shown in Fig. 2. AgI exhibited type II isotherms without significant hysteresis loop and no pores existed (the inset of Fig. 2). However, $Bi_2O_2CO_3$ and AgI/$Bi_2O_2CO_3$ showed type II isotherms with a H3 hysteresis loop associated with the assemblages of platelike particles, leading to plenty of mesopores and macropores within a wide range of pore diameter (the inset of Fig. 2) [22]. Compared to that of $Bi_2O_2CO_3$, the hysteresis loop of AgI/$Bi_2O_2CO_3$ was broadened, indicating the generation of more interstitial spaces between the platelike particles [22]. These results were consistent with the SEM observations. The BET surface area of AgI/$Bi_2O_2CO_3$ (16.00 $m^2 g^{-1}$) was larger than AgI (6.31 $m^2 g^{-1}$) and $Bi_2O_2CO_3$ (13.87 $m^2 g^{-1}$). The enlarged surface area of AgI/$Bi_2O_2CO_3$ was likely due to the flower-like morphology from nanoplates.

The TEM image of AgI/$Bi_2O_2CO_3$ (Fig. S2A) showed that numerous nanoparticles around 5–20 nm was observed on the surface of the plate-like particles. The HRTEM (Fig. S2B) further exhibited that the plate-like particles with lattice fringes at 0.30 nm corresponded to the (013) d-spacing of $Bi_2O_2CO_3$, whereas some of the nanoparticles on the surface of $Bi_2O_2CO_3$ with lattice fringes at 0.38 nm and 0.27 nm attributed to the corresponding plane of β/γ-AgI, confirming AgI nanoparticles dispersed on the surface of $Bi_2O_2CO_3$ thin sheets.

The XRD patterns of the different samples were shown in Fig. 3. The diffraction peaks of $Bi_2O_2CO_3$ could be indexed to tetragonal $Bi_2O_2CO_3$ (JCPDS 41-1448). The diffraction peaks of AgI was contributed to β/γ-AgI. The indexed diffraction peaks of AgI/$Bi_2O_2CO_3$ could be ascribed to β/γ-AgI and $Bi_2O_2CO_3$. In $Bi_2O_2CO_3$, these peaks for (002), (004), and (006) belonging to the {001} facets exhibited much higher intensities than most of the other peaks, indicating that the major exposed surfaces of $Bi_2O_2CO_3$ were {001}

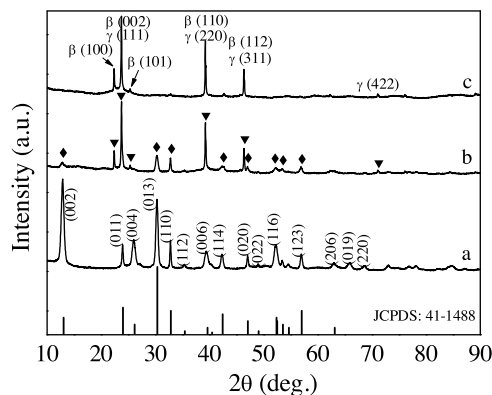facets [12]. However, these peaks in AgI/$Bi_2O_2CO_3$ was significantly reduced, and the intensity ratio of the (110) peak to the (013) peak was obviously larger, indicating that $Bi_2O_2CO_3$ in AgI/$Bi_2O_2CO_3$ was preferentially oriented along the {110} crystallographic plane [13]. In the crystal structure of the $Bi_2O_2CO_3$, Bi-O layers and (CO_3) layers were intergrown with the plane of the (CO_3) group orthogonal to the plane of the Bi-O layer. The large cation Bi^{3+} with [8]-coordination showed stereo active lone-pair behaviors that may result in the Bi-O polyhedron with large distortion [23]. On the preferentially exposed {001} plane of $Bi_2O_2CO_3$, the Bi-O square anti-prism with [8]-coordination compressed along the c-axis supplied lots of defects formed from the unstable oxygen which have the unstable bond with the Bi atoms. The high oxygen characteristic of the $Bi_2O_2CO_3$ {001} facets could provide active sites to bond with AgI [21]. Therefore, AgI mainly coverred on the {001} facets of $Bi_2O_2CO_3$ reducing their exposure ratio in AgI/$Bi_2O_2CO_3$ [10].

The structure of AgI/$Bi_2O_2CO_3$ was further studied using FTIR spectroscopy (Fig. 4). Four characteristic band groups of CO_3^{2-} in $Bi_2O_2CO_3$ were observed, including symmetric stretching mode ν1 at 1067 cm^{-1}, out-of-plane bending mode ν2 at 847 and 821 cm^{-1}, anti-symmetric mode ν3 at 1474 and 1389 cm^{-1}, in-plane deformation ν4 at 690 and 669 cm^{-1}, and ν1 + ν4 at 1755 and 1736 cm^{-1} [15]. The symmetric stretching mode ν1 and in-plane deformation ν4 of CO_3^{2-} were not observed in AgI/$Bi_2O_2CO_3$. The intensities of all other peaks significantly deceased in AgI/$Bi_2O_2CO_3$, and the band group at 1474 and 1389 cm^{-1} red-shifted to 1470 and 1385 cm^{-1}. The results indicated the significant change of chemical environments of CO_3^{2-} after in-situ combining $Bi_2O_2CO_3$ with AgI.

As shown in Fig. 5, the two XPS characteristic peaks for Bi 4f in $Bi_2O_2CO_3$ located at 159.2 and 164.5 eV were attributed to Bi $4f_{7/2}$ and Bi $4f_{5/2}$ of Bi^{3+} [24]. These peaks in AgI/$Bi_2O_2CO_3$ were shifted up by 0.4 eV. Moreover, the peaks of O 1s at 530.0, 531.0, and 531.4 eV, which can be assigned to Bi-O, carbonate and the absorbed hydroxyl in $Bi_2O_2CO_3$, respectively, were also shifted up by about

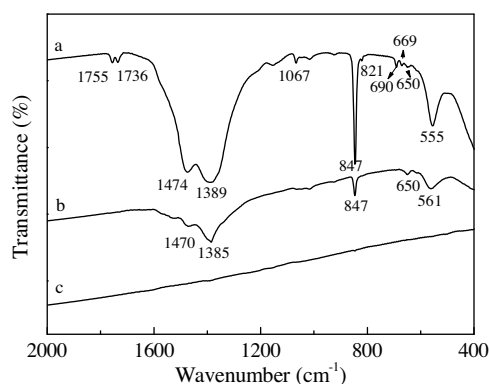**Fig. 4.** IR spectra of (a) $Bi_2O_2CO_3$, (b) $AgI/Bi_2O_2CO_3$, and (c) AgI.

0.4 eV in $AgI/Bi_2O_2CO_3$. Consequently, compared to $Bi_2O_2CO_3$, the binding energies of both Bi and O atoms in $AgI/Bi_2O_2CO_3$ shifted positively, indicating the presence of strong interactions between $Bi_2O_2CO_3$ and AgI, which led to alternate the distribution of the electric charge of Bi and O atoms in the composite. In the C 1s spectra, the peak at 288.8 eV ascribing to carbonate ion in $Bi_2O_2CO_3$

were shifted up to 289.3 eV after in-situ combining with AgI, while other peaks assigning to adventitious carbon species from XPS measurements kept unchanged. Therefore, the strong interaction between $Bi_2O_2CO_3$ and AgI could influence the electronic distribution of C in the CO_3^{2-} layers as well. The Ag $3d_{5/2}$ and Ag $3d_{3/2}$ peaks of AgI were centered at 368.8 and 374.8 eV, respectively, characteristics of Ag^+ species. The two characteristic peaks were shifted down by 0.3 eV in $AgI/Bi_2O_2CO_3$. Similarly, the I $3d_{5/2}$ and I $3d_{3/2}$ peaks of AgI at 620.1 and 631.5 eV were shifted down by 0.4 eV in $AgI/Bi_2O_2CO_3$. The negative shift of the binding energies of both Ag and I atoms in $AgI/Bi_2O_2CO_3$ confirmed the strong effect of $Bi_2O_2CO_3$ on AgI, which led to alternate the distribution of the electric charge of Ag and I atoms in the composite. In addition, the Auger parameter (α'), which was defined as the sum of the kinetic energy of the Auger elecron (Ag M_4VV) and the binding energy of the core level (Ag $3d_{5/2}$), was further calculated to be 724.3 and 724.2 eV for AgI and $AgI/Bi_2O_2CO_3$, respectively, confirming no metallic Ag^{00} was present [25,26]. Therefore, the in-situ close connection of $Bi_2O_2CO_3$ and AgI altered the charge distribution of $Bi_2O_2CO_3$ and AgI, and chemical bond was formed at the interface of $Bi_2O_2CO_3$ and AgI.

The optical properties of different samples were shown in Fig. 6, including nitrogen-doped TiO_2 ($TiO_{2-x}N_x$), which is considered the
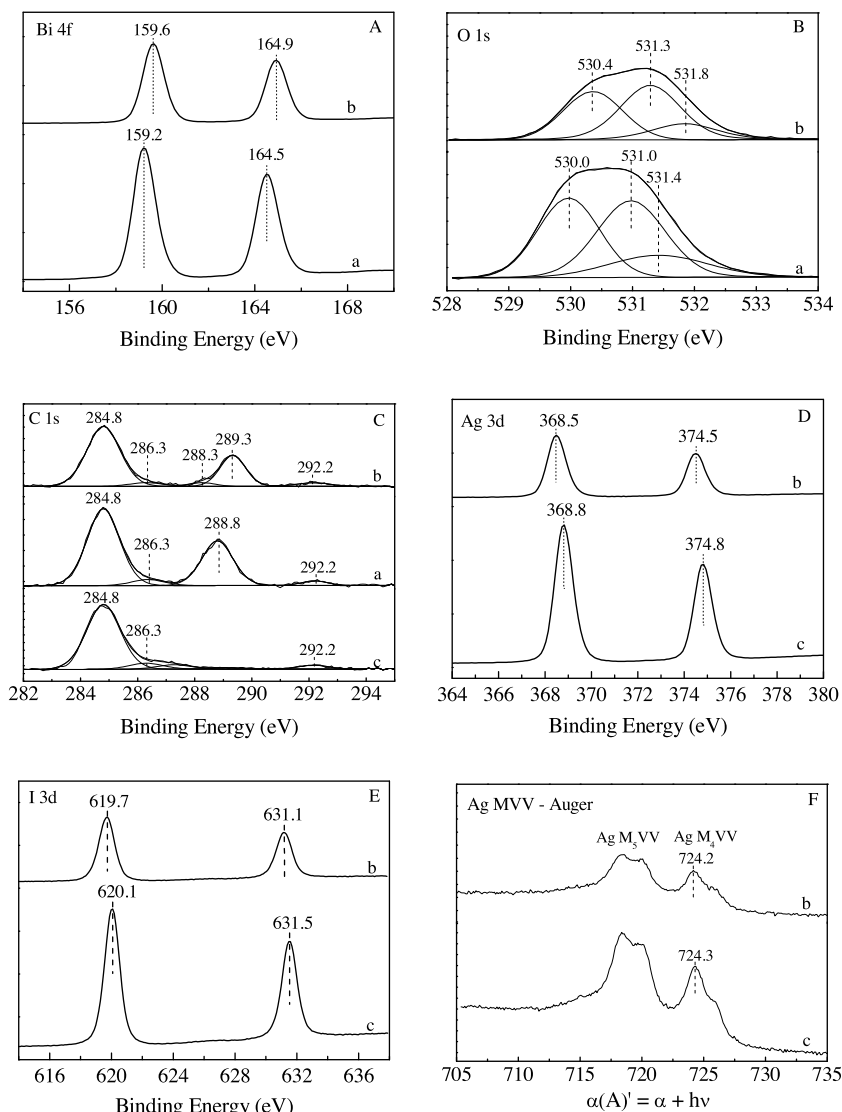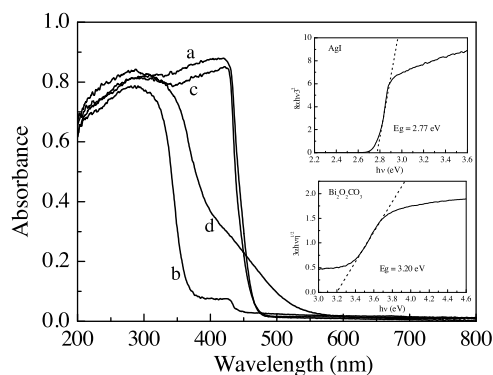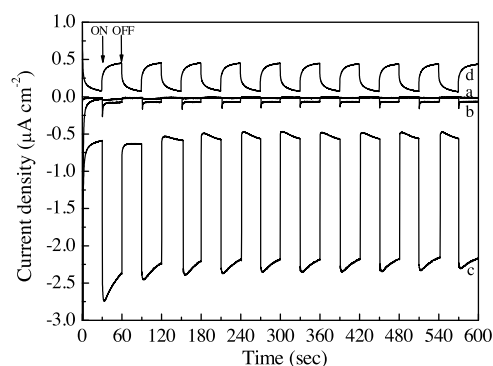

Fig. 5. XPS spectra of (a) $Bi_2O_2CO_3$, (b) $AgI/Bi_2O_2CO_3$ and (c) AgI: (A) Bi 4f, (B) O 1s, (C) C 1s, (D) Ag 3d, (E) I 3d, and (F) Ag MVV-Auger.

Fig. 6. UV–vis diffuse reflectance spectra of (a) AgI, (b) $Bi_2O_2CO_3$, (c) AgI/$Bi_2O_2CO_3$, and (d) $TiO_{2-x}N_x$. The inset is the Tauc's plots of AgI and $Bi_2O_2CO_3$.

Fig. 7. Transient photocurrent response of (a) $Bi_2O_2CO_3$, (b) AgI, (c) AgI/$Bi_2O_2CO_3$, and (d) $TiO_{2-x}N_x$ under visible light irradiation ($\lambda > 400$ nm).

standard example of a visible-light photocatalyst prepared as a reference [27]. $Bi_2O_2CO_3$ performed a 385 nm absorption band-edge in the UV region, and AgI absorbed sunlight with wavelengths less than 480 nm. Spectra of AgI/$Bi_2O_2CO_3$ was similar with AgI, further confirming no metallic Ag^{00} was present in AgI/$Bi_2O_2CO_3$. For a crystalline semiconductor, the optical absorption near band edge followed the equation $\alpha h\upsilon = A(h\upsilon - Eg)^{n/2}$, where α, υ, Eg and A are absorption coefficient, light frequency, band gap energy, and a constant, respectively [28]. The value of n decided the characteristics of the transition in a semiconductor (n = 1 for direct transition and n = 4 for indirect transition). The n for $Bi_2O_2CO_3$ and AgI were 4 and 1, respectively. Therefore, the Eg of $Bi_2O_2CO_3$ and AgI were approximately 3.20 eV and 2.77 eV, respectively.

3.2. Photoelectrochemical measurements

Representative current density versus voltage (I–V) characteristics of different catalysts were presented in Fig. S3. Compared with the pure AgI and $Bi_2O_2CO_3$, a significant increase in the photocurrent density was observed across the potential window for AgI/$Bi_2O_2CO_3$ under visible light irradiation (Fig. S3A). The performance of AgI/$Bi_2O_2CO_3$ under visible light was much better than in the dark as expected (Fig. S3B). Furthermore, the transient photocurrent responses of $Bi_2O_2CO_3$, AgI and AgI/$Bi_2O_2CO_3$ were recorded via several on-off cycles of irradiation to give furher evidence for the visible light activity of AgI/$Bi_2O_2CO_3$. As shown in Fig. 7, prompt generation of photocurrent can be observed for AgI/$Bi_2O_2CO_3$ upon illumination with visible light. The rise and fall of the photo-current corresponded well to the illumination being switched on and off. And the photocurrent density of AgI/$Bi_2O_2CO_3$ and AgI was about 2 μA cm^{-2} and 0.1 μA cm^{-2}, respectively, whereas that of $Bi_2O_2CO_3$ was almost zero. As a ref-
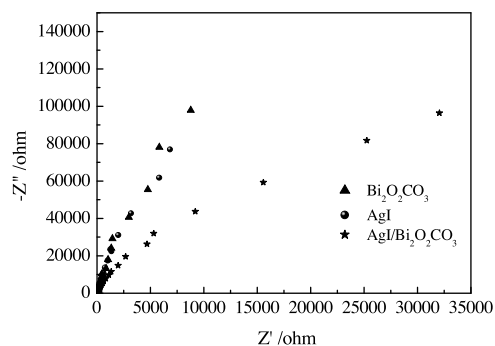
Fig. 8. EIS Nyquist plots of $Bi_2O_2CO_3$, AgI and AgI/$Bi_2O_2CO_3$ under visible light irradiation.

erence, the photocurrent density of $TiO_{2-x}N_x$ was also measured to be 0.35 μA cm^{-2} at the similar conditions. The photoconversion efficiency, η, of light energy to chemical energy in the presence of an external applied potential, E_{app}, can be calculated as: η (%) = j_p [$E_{rev} - |E_{app}|] \times 100/I_0$ [29], where j_p is the photocurrent density (mA cm^{-2}), E_{rev} is the standard state-reversible potential (which is 1.23 V vs. NHE). E_{app} is the applied potential derived from: $E_{app} = E_{meas} - E_{aoc}$, where E_{meas} is the electrode potential of the working electrode at which the photocurrent was measured under illumination and E_{aoc} is the electrode potential of the same working electrode under open circuit conditions, under the same illumination, and in the same electrolyte. In addition, I_0 is the power density of incident light (mW cm^{-2}). E_{aoc} of AgI, AgI/$Bi_2O_2CO_3$ and $TiO_{2-x}N_x$ under visible light illumination was 0.045, 0.34 and −0.44 V vs. SCE (Fig. S4), respectively. Without adding the bias voltage, the photoconversion efficiency of AgI/$Bi_2O_2CO_3$ was calculated as 5.09%, which was 15 times higher than that of AgI (0.34%) and 6.4 times higher than that of $TiO_{2-x}N_x$ (0.79%) under the same conditions.

The radius of the arc on the EIS Nyquist plot could reflect the reaction rate occurring at the surface of catalysts. The arc radius of AgI/$Bi_2O_2CO_3$ was smaller than that of $Bi_2O_2CO_3$ or AgI under visible light irradiation (Fig. 8), suggesting that the close contact of $Bi_2O_2CO_3$ and AgI led to a more effective separation of photogenerated electron-hole pairs and faster interfacial charge transfer. All the above results proved that the formed *p-n* heterojunction can promote the separation and transfer of photo-generated electrons, inhibiting the recombination of electrons and holes effectively.

3.3. Photocatalytic performance

To evaluate the photocatalytic activity and stability of the catalysts, the degradation of 2-CP was carried out in aqueous dispersions at room temperature and neutral pH after the adsorption equilibrium of 2-CP in dark. After being stirred in the dark for 30 min, the adsorption capacities of AgI, $Bi_2O_2CO_3$ and AgI/$Bi_2O_2CO_3$ to 2-CP were 0.7%, 0.7% and 2.3%, respectively. Therefore, AgI/$Bi_2O_2CO_3$ with the largest BET surface area (16.00 m^2 g^{-1}) showed the highest adsorption capacity. The adsorption and reaction solution pH was nearly neutral (around 6.6). The isoelectric points of AgI, $Bi_2O_2CO_3$ and AgI/$Bi_2O_2CO_3$ were determined to be pH 3.1, 3.8 and 3.4, respectively, according to the measurement of zeta potentials (Fig. S5). Thus, the surface of AgI, $Bi_2O_2CO_3$ and AgI/$Bi_2O_2CO_3$ are negatively charged. 2-CP is dominantly present in the molecular form (pKa = 8.56) [30], and thus 2-CP is not adsorbed on the surface of the photocatalysts via electrostatic interaction at nearly neutral pH. As shown in Fig. 9, under visible light irradiation, no significant degradation of 2-CP was detected in $Bi_2O_2CO_3$ suspension. The degradation of 2-CP within 60 min was about 20%, 31%, and 35% in the AgI, $TiO_{2-x}N_x$, and AgI + $Bi_2O_2CO_3$ (i.e. the physical mixture of AgI and $Bi_2O_2CO_3$ with the same ratio as AgI/$Bi_2O_2CO_3$)
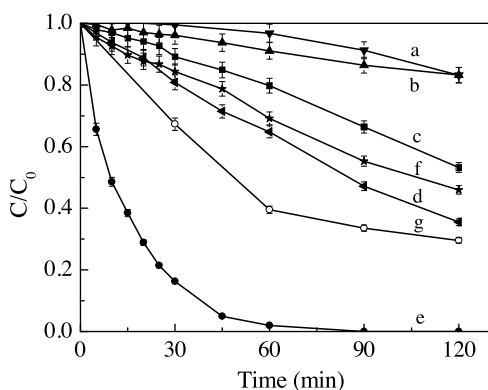
Fig. 9. Degradation of 2-CP ($10\,mg\,L^{-1}$) in different suspensions ($1.6\,g\,L^{-1}$) under visible light ($\lambda > 400\,nm$): (a) no catalyst added, (b) $Bi_2O_2CO_3$, (c) AgI, (d) AgI + $Bi_2O_2CO_3$, (e) AgI/$Bi_2O_2CO_3$, (f) $TiO_{2-x}N_x$, and (g) TOC removal of 2-CP in AgI/$Bi_2O_2CO_3$ suspension.

Fig. 10. Degradation of 2-CP in AgI/$Bi_2O_2CO_3$ suspension ($1.6\,g\,L^{-1}$) under visible light ($\lambda > 400\,nm$) with (a) no scavenger added, (b) N_2-bubbling, (c) 0.1 M t-butanol, (d) 5 mM $K_2S_2O_8$, (e) 1 mM triethanolamine, and (f) 1 mM p-benzoquinone.

suspensions, respectively. In AgI/$Bi_2O_2CO_3$ suspension, the degradation rate of 2-CP significantly increased and up to 98% of 2-CP was removed within 60 min under the same conditions, which was 4.9, 3.2, and 2.8 times faster than that in AgI, $TiO_{2-x}N_x$, and AgI + $Bi_2O_2CO_3$ suspensions, respectively. And the TOC removal rate of 2-CP was more than 70% within 120 min in AgI/$Bi_2O_2CO_3$ suspension. The IC profiles of the released ions during the degradation of 2-CP were presented in Fig. S6. The generation of Cl^- was observed. The additional peaks in the IC profiles revealed the generation of small molecular organic acids and the further interaction of released chloride ions either with reactive oxygen species or the photogenerated holes into other Cl containing off shoots such as ClO_2^-, ClO_3^- and ClO_4^- [31,32]. ClO_3^- was identified by comparing the retention time with standard compounds in this study. After reaction for 60 min, 0.006 mM Cl^- and 0.028 mM ClO_3^- was generated from 0.078 mM 2-CP. And 0.0014 mM Cl^- and 0.037 mM ClO_3^- was generated at 120 min. These results indicated the concentration reduction of 2-CP was a result of mineralization rather than adsorption. In the whole reaction process, the release of Ag^+ and Bi^{3+} was hardly detected in the solution by ICP-OES. The cycle tests exhibited that the conversion of 2-CP remained at approximately 88% within 60 min after seven continuous cycles (Fig. S7). Furthermore, no phase change was observed in the XRD pattern of AgI/$Bi_2O_2CO_3$ after reaction (Fig. S8). The XPS spectra of surface Bi, O, C, Ag and I of AgI/$Bi_2O_2CO_3$ remained intact after reaction (Fig. S9), except for the occurrence of O 1s peak at 533.5 eV assigned to the loosely bound oxygen on solid surface after oxidizing pollutants. The results indicated that AgI/$Bi_2O_2CO_3$ had an excellent stability. The high activity and stability of AgI/$Bi_2O_2CO_3$ were probably related to its well-organized morphology and the interfacial structures. The larger surface area of AgI/$Bi_2O_2CO_3$ and the smaller particle of AgI in AgI/$Bi_2O_2CO_3$ than the pure $Bi_2O_2CO_3$ or AgI enhanced its surface reactivity, and the close contact between $Bi_2O_2CO_3$ and AgI by in-situ cocrystalization could facilitate the interfacial charge transfer more efficiently.

3.4. Photocatalytic mechanism

To elucidate the photocatalytic mechanism of AgI/$Bi_2O_2CO_3$ under visible light irradiation, the effects of various radical scavengers on the degradation of 2-CP were examined in Fig. 10. Under the addition of the superoxide ($O_2^{\bullet-}$) scavenger p-benzoquinone and hole (h^+) scavenger triethanolamine, only about 15% and 29% of 2-CP was degraded in AgI/$Bi_2O_2CO_3$ suspension under visible light ($\lambda > 400\,nm$) within 60 min. Since the addition of 1 mM triethanolamine significantly changed the solution pH from 6.6 to 8.9, a control experiment with adjusted pH showed that the changed
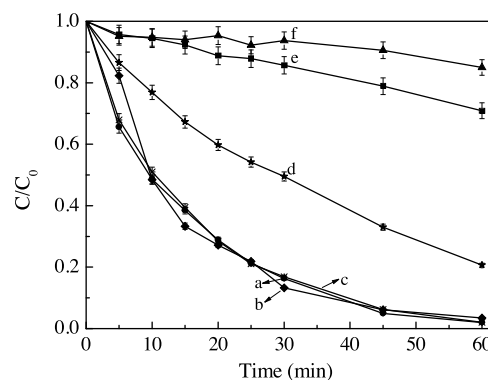
pH slightly influenced the degradation rate of 2-CP (Fig. S10), indicating the significant h^+ scavengering effect of triethanolamine. In addition, there was about 79% of 2-CP that was photodegraded with the addition of electron (e^-) scavenger $K_2S_2O_8$. However, the degradation rate of 2-CP was hardly changed with the addition of hydroxyl radicals ($^\bullet OH$) scavenger t-butanol. Furthermore, the BMPO spin-trapping ESR technique was used to detect OH and $O_2^{\bullet-}$ production (Fig. S11). No characteristic peaks of BMPO-$^\bullet OH$ were observed in AgI/$Bi_2O_2CO_3$ suspension under visible light irradiation, suggesting that $^\bullet OH$ oxidation was not the main reaction during photocatalytic process. In fact, the valence band edge potential of AgI was determined at 2.235 eV by Mulliken electronegativity theory: $E_{VB} = X - E^e + 0.5\,E_g$, where X was the electronegativity of the semiconductor, defined as the geometric mean of the absolute electronegativity of the constituent atoms, E^e was the energy of free electrons on the hydrogen scale (4.5 eV), and E_g was the band gap of the semiconductor. The value was less positive than the standard reduction potential of $^\bullet OH/OH-$ (2.38 eV) [33,34], confirming that the h^+ on the surface of AgI cannot oxidize OH− into $^\bullet OH$ kinetically. The characterization peaks of BMPO-$O_2^{\bullet-}$ were obviously observed in AgI/$Bi_2O_2CO_3$ suspension under visible light irradiation, while little $O_2^{\bullet-}$ was detected in dark. Based on the above results, the photocatalytic process was mainly governed by the superoxide and the holes rather than the hydroxyl radicals, and e^- was also in part responsible for the degradation of 2-CP. Specially, the degradation rate of 2-CP was not changed under N_2 atmosphere without any sacrificial reagent, indicating the superoxide probably came from the reaction of e^- and surface adsorbed O_2. This may also demonstrate that $Bi_2O_2CO_3$ in the composite acted to suppress the recombination of e^-/h^+ pairs by promoting photogenerated electrons away from the AgI surface, which was independent on the existence of O_2 in solution [35].

The match of band structures was important for highly active and stable composite semiconductor photocatalysts [8]. The VB XPS spectra of $Bi_2O_2CO_3$ and AgI were measured in Fig. 11. By extrapolating the leading edge of the VB to its intersection with background counts near the Fermi level, the position of the Fermi level with respect to the valence band maximum (VBM) could be determined [36]. The Fermi level was located at 2.11 eV above the VBM for the $Bi_2O_2CO_3$, whereas it was 1.25 eV for the AgI. Since the E_g of $Bi_2O_2CO_3$ and AgI were 3.20 eV and 2.77 eV, respectively, the Fermi level of $Bi_2O_2CO_3$ was near the CBM and that of AgI was near the VBM, confirming the n-type characteristic of $Bi_2O_2CO_3$ and the p-type characteristic of AgI. The Mott-Schottky plot of $Bi_2O_2CO_3$ with a positive slope (Fig. S12) also indicated the n-type characteristic of $Bi_2O_2CO_3$ [37]. In comparison with the XPS spectra of the pure $Bi_2O_2CO_3$ and AgI, the positive shift in the binding energy of Bi 4f, O 1s and C 1s for carbonate and the negative shift in the

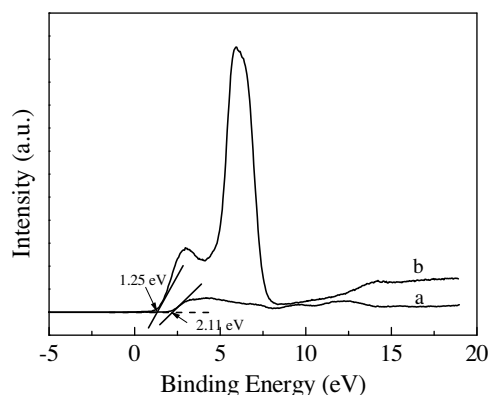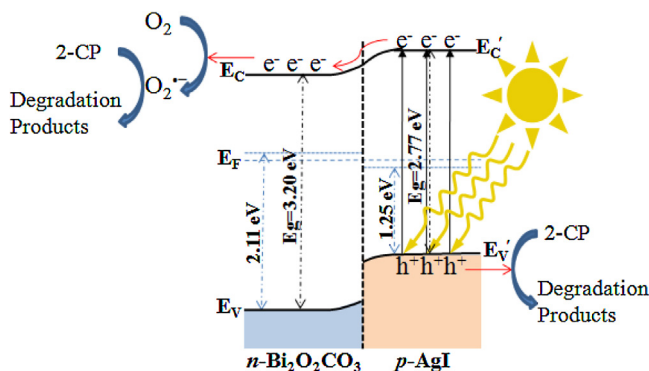**Fig. 11.** VB XPS spectra of the catalysts: (a) $Bi_2O_2CO_3$, and (b) AgI.

Scheme 1. Proposed photocatalytic mechanism for AgI/$Bi_2O_2CO_3$.

4. Conclusions

The p-AgI/n-$Bi_2O_2CO_3$ heterojunction was successfully prepared by a one-step co-crystallization method. The visible-light-driven photoactivity of AgI was enhanced by nearly 5 times through in-situ close contact with $Bi_2O_2CO_3$ under ambient conditions. The characterization results showed p-AgI nanoparticles dispersedly anchored on {001} facets of layered n-$Bi_2O_2CO_3$ sheets, increasing the BET surface area of the composite and decreasing the particle size of AgI. The strong interfacial interactions in p-AgI/n-$Bi_2O_2CO_3$ promoted the transfer of the photo-generated electrons from AgI to $Bi_2O_2CO_3$ to generate $O_2^{\bullet-}$ by reducing the surface chemisorbed O_2. The synergistic effect of $O_2^{\bullet-}$ and the photo-generated holes led to the fast and stable degradation and mineralization of 2-CP. These results suggest that AgI/$Bi_2O_2CO_3$ is a promising visible-light-sensitive photocatalyst for removal of organic pollutants in wastewater.

Appendix A. Supplementary data

Supplementary data associated with this article can be found, in the online version, at http://dx.doi.org/10.1016/j.apcatb.2016.12.015.

binding energy of Ag 3d and I 3d in AgI/$Bi_2O_2CO_3$ demonstrated the down-shifting of the Fermi level of $Bi_2O_2CO_3$ and the up-shifting of the Fermi level of AgI after close contact of $Bi_2O_2CO_3$ and AgI [38]. The p-AgI and n-$Bi_2O_2CO_3$ semiconductors normally had different positions of the Fermi levels when they were separated or preequilibrium. When p-AgI and n-$Bi_2O_2CO_3$ semiconductors formed p-n heterojunction in dark, both AgI and $Bi_2O_2CO_3$ semiconductors had the same Fermi level after the charge equilibrium being built [11]. On the other hand, the higher Fermi energy of n-$Bi_2O_2CO_3$ than p-AgI caused the energy bands of n-$Bi_2O_2CO_3$ to bend upward and p-AgI to bend downward toward the interface after the two semiconductors were in contact and to reach electrical equilibrium [39]. Therefore, the band structure of AgI and $Bi_2O_2CO_3$ in AgI/$Bi_2O_2CO_3$ could be obtained as shown in Scheme 1. Under visible light illumination ($\lambda > 400$ nm), only AgI in AgI/$Bi_2O_2CO_3$ can be photoexcited, the photogenerated electrons of the CB of AgI would transfer to the CB of $Bi_2O_2CO_3$ to reduce the surface chemisorbed O_2 into the strong oxidizing species $O_2^{\bullet-}$, while the photogenerated holes of the VB of AgI could directly oxidize organic pollutants into small moleculars, owing to the built-in potential in the AgI/$Bi_2O_2CO_3$ p-n heterojunction. Therefore, the photogenerated carriers could be efficiently separated and the photogenerated holes (electrons) would be concentrated on the AgI ($Bi_2O_2CO_3$) and consumed, resulting in the high photoactivity of the p-AgI/n-$Bi_2O_2CO_3$ heterojunction catalyst to degrade organic pollutants. In addition, since the photogenerated electrons preferably drifted to the $Bi_2O_2CO_3$ side, AgI in AgI/$Bi_2O_2CO_3$ p-n heterojunction may avoid being photoreduced to Ag, leading to better stability under visible illumination.

References

[1] H. Wang, L. Zhang, Z. Chen, J. Hu, S. Li, Z. Wang, J. Liu, X. Wang, Semiconductor heterojunction photocatalysts: design, construction, and photocatalytic performances, Chem. Soc. Rev. 43 (2014) 5234–5244.
[2] C. Yu, G. Li, S. Kumar, K. Yang, R. Jin, Phase transformation synthesis of novel Ag_2O/Ag_2CO_3 heterostructures with high visible light efficiency in photocatalytic degradation of pollutants, Adv. Mater. 26 (2014) 892–898.
[3] Z. Jiang, W. Wei, D. Mao, C. Chen, Y. Shi, X. Lv, J. Xie, Silver-loaded nitrogen-doped yolk-shell mesoporous TiO_2 hollow microspheres with enhanced visible light photocatalytic activity, Nanoscale 7 (2015) 784–797.
[4] H. Huang, X. Li, J. Wang, F. Dong, P.K. Chu, T. Zhang, Y. Zhang, Anionic group self-doping as a promising strategy: band-gap engineering and multi-functional applications of high-performance CO_3^{2-}-doped $Bi_2O_2CO_3$, ACS Catal. 5 (2015) 4094–4103.
[5] X. Chen, C. Burda, The electronic origin of the visible-light absorption properties of C–, N– and S-doped TiO_2 nanomaterials, J. Am. Chem. Soc. 130 (2008) 5018–5019.
[6] Y. Qu, X. Duan, Progress, challenge and perspective of heterogeneous photocatalysts, Chem. Soc. Rev. 42 (2013) 2568–2580.
[7] S.Y. Chai, Y.J. Kim, M.H. Jung, A.K. Chakraborty, D. Jung, W.I. Lee, Heterojunctioned BiOCl/Bi_2O_3, a new visible light photocatalyst, J. Catal. 262 (2009) 144–149.
[8] L. Kong, Z. Jiang, H.H. Lai, R.J. Nicholls, T. Xiao, M.O. Jones, P.P. Edwards, Unusual reactivity of visible-light-responsive AgBr–BiOBr heterojunction photocatalysts, J. Catal. 293 (2012) 116–125.
[9] L. Chen, D. Jiang, T. He, Z. Wu, M. Chen, In-situ ion exchange synthesis of hierarchical AgI/BiOI microsphere photocatalyst with enhanced photocatalytic properties, CrystEngComm 15 (2013) 7556–7563.
[10] H. Huang, K. Xiao, K. Liu, S. Yu, Y. Zhang, Composition-transforming fabrication of BiOI/$BiOIO_3$ heterostructure: semiconductor p–n junction and dominantly exposed reactive facets, Cryst. Growth Des. 16 (2016) 221–228.
[11] N. Liang, M. Wang, L. Jin, S. Huang, W. Chen, M. Xu, Q. He, J. Zai, N. Fang, X. Qian, Highly efficient Ag_2O/$Bi_2O_2CO_3$ p-n heterojunction photocatalysts with improved visible-light responsive activity, ACS Appl. Mater. Interfaces 6 (2014) 11698–11705.
[12] H. Huang, J. Wang, F. Dong, Y. Guo, N. Tian, Y. Zhang, T. Zhang, Highly efficient $Bi_2O_2CO_3$ single-crystal lamellas with dominantly exposed {001} facets, Cryst. Growth Des. 15 (2015) 534–537.
[13] S. Peng, L. Li, H. Tan, Y. Wu, R. Cai, H. Yu, X. Huang, P. Zhu, S. Ramakrishna, M. Srinivasan, Q. Yan, Monodispersed Ag nanoparticles loaded on the PVP-assisted synthetic $Bi_2O_2CO_3$ microspheres with enhanced photocatalytic and supercapacitive performances, J. Mater. Chem. A 1 (2013) 7630–7638.
[14] F. Dong, Q. Li, Y. Sun, W.K. Ho, Noble metal-like behavior of plasmonic Bi particles as a cocatalyst deposited on $(BiO)_2CO_3$ microspheres for efficient visible light photocatalysis, ACS Catal. 4 (2014) 4341–4350.

[15] F. Dong, Y. Sun, M. Fu, W.K. Ho, S.C. Lee, Z. Wu, Novel in situ N-doped (BiO)$_2$CO$_3$ hierarchical microspheres self-assembled by nanosheets as efficient and durable visible light driven photocatalyst, Langmuir 28 (2012) 766–773.

[16] Y.S. Xu, W.D. Zhang, Anion exchange strategy for construction of sesame-biscuit-like Bi$_2$O$_2$CO$_3$/Bi$_2$MoO$_6$ nanocomposites with enhanced photocatalytic activity, Appl. Catal. B: Environ. 140–141 (2013) 306–316.

[17] L. Chen, S.F. Yin, S.L. Luo, R. Huang, Q. Zhang, T. Hong, P.C.T. Au, Bi$_2$O$_2$CO$_3$/BiOI photocatalysts with heterojunctions highly efficient for visible-light treatment of dye-containing wastewater, Ind. Eng. Chem. Res. 51 (2012) 6760–6768.

[18] N. Liang, J. Zai, M. Xu, Q. Zhu, X. Wei, X. Qian, Novel Bi$_2$S$_3$/Bi$_2$O$_2$CO$_3$ heterojunction photocatalysts with enhanced visible light responsive activity and wastewater treatment, J. Mater. Chem. A 2 (2014) 4208–4216.

[19] F. Chen, Q. Yang, C. Niu, X. Li, C. Zhang, J. Zhao, Q. Xu, Y. Zhong, Y. Deng, G. Zeng, Enhanced visible light photocatalytic activity and mechanism of ZnSn(OH)$_6$ nanocubes modified with AgI nanoparticles, Catal. Commun. 73 (2016) 1–6.

[20] H. Cheng, W. Wang, B. Huang, Z. Wang, J. Zhan, X. Qin, X. Zhang, Y. Dai, Tailoring AgI nanoparticles for the assembly of AgI/BiOI hierarchical hybrids with size-dependent photocatalytic activities, J. Mater. Chem. A 1 (2013) 7131–7136.

[21] Z. Zhao, Y. Zhou, F. Wang, K. Zhang, S. Yu, K. Cao, Polyaniline-decorated {001} facets of Bi$_2$O$_2$CO$_3$ nanosheets: in situ oxygen vacancy formation and enhanced visible light photocatalytic activity, ACS Appl. Mater. Interfaces 7 (2015) 730–737.

[22] J.W. Liu, Y. Zhang, X.W. Chen, J.H. Wang, Graphene oxide–rare earth metal–organic framework composites for the selective isolation of hemoglobin, ACS Appl. Mater. Interfaces 6 (2014) 10196–10204.

[23] Y. Zheng, F. Duan, M. Chen, Y. Xie, Synthetic Bi2O2CO3 nanostructure: novel photocatalyst with controlled special surface exposed, J. Mol. Catal. A: Chem. 317 (2010) 34–40.

[24] P. Madhusudan, J. Zhang, B. Cheng, G. Liu, Photocatalytic degradation of organic dyes with hierarchical Bi$_2$O$_2$CO$_3$ microstructures under visible-light, CrystEngComm 15 (2013) 231–240.

[25] J. Chen, X. Tang, J. Liu, E. Zhan, J. Li, X. Huang, W. Shen, Synthesis and characterization of Ag-hollandite nanofibers and its catalytic application in ethanol oxidation, Chem. Mater. 19 (2007) 4292–4299.

[26] S.G. Aspromonte, M.D. Mizrahi, F.A. Schneeberger, J.M.R. López, A.V. Boix, Study of the nature and location of silver in Ag-exchanged mordenite catalysts, characterization by spectroscopic techniques, J. Phys. Chem. C 117 (2013) 25433–25442.

[27] A.I. Kontos, A.G. Kontos, Y.S. Raptis, P. Falaras, Nitrogen modified nanostructured titania: electronic, structural and visible-light photocatalytic properties, Phys. Status Solidi (RRL). 2 (2008) 83–85.

[28] H. Lin, J. Cao, B. Luo, B. Xu, S. Chen, Synthesis of novel Z-scheme AgI/Ag/AgBr composite with enhanced visible light photocatalytic activity, Catal. Commun. 21 (2012) 91–95.

[29] S.U.M. Khan, M. Al-Shahry, W.B. Ingler, Efficient photochemical water splitting by a chemically modified n-TiO$_2$, Science 297 (2002) 2243–2245.

[30] Y.H. Chuang, Y.M. Tzou, M.K. Wang, C.H. Liu, P.N. Chiang, Removal of 2-chlorophenol from aqueous solution by Mg/Al layered double hydroxide (LDH) and modified LDH, Ind. Eng. Chem. Res. 47 (2008) 3813–3819.

[31] N. Salah, A. Hameed, M. Aslam, M.S. Abdel-wahab, S.S. Babkair, F.S. Bahabri, Flow controlled fabrication of N doped ZnO thin films and estimation of their performance for sunlight photocatalytic decontamination of water, Chem. Eng. J. 291 (2016) 115–127.

[32] M.T. Qamar, M. Aslam, I.M.I. Ismail, N. Salah, A. Hameed, The assessment of the photocatalytic activity of magnetically retrievable ZnO coated γ-Fe$_2$O$_3$ in sunlight exposure, Chem. Eng. J. 283 (2016) 656–667.

[33] H. Cheng, B. Huang, Y. Dai, X. Qin, X. Zhang, One-step synthesis of the nanostructured AgI/BiOI composites with highly enhanced visible-light photocatalytic performances, Langmuir 26 (2010) 6618–6624.

[34] J. Cao, B. Xu, B. Luo, H. Lin, S. Chen, Preparation, characterization and visible-light photocatalytic activity of AgI/AgCl/TiO$_2$, Appl. Surf. Sci. 257 (2011) 7083–7089.

[35] H. Adamu, P. Dubey, J.A. Anderson, Probing the role of thermally reduced graphene oxide in enhancing performance of TiO$_2$ in photocatalytic phenol removal from aqueous environments, Chem. Eng. J. 284 (2016) 380–388.

[36] Q. Zhu, W.S. Wang, L. Lin, G.Q. Gao, H.L. Guo, H. Du, A.W. Xu, Facile synthesis of the novel Ag3VO4/AgBr/Ag plasmonic photocatalyst with enhanced photocatalytic activity and stability, J. Phys. Chem. C 117 (2013) 5894–5900.

[37] H. Wang, J. Chen, F. Xiao, J. Zheng, B. Liu, Doping-induced structural evolution from rutile to anatase: formation of Nb-doped anatase TiO2 nanosheets with high photocatalytic activity, J. Mater. Chem. A 4 (2016) 6926–6932.

[38] H. Tan, Z. Zhao, W. Zhu, E.N. Coker, B. Li, M. Zheng, W. Yu, H. Fan, Z. Sun, Oxygen vacancy enhanced photocatalytic activity of pervoskite SrTiO3, ACS Appl. Mater. Interfaces 6 (2014) 19184–19190.

[39] Z. Zhang, J.T. Yates, Band bending in semiconductors: chemical and physical consequences at surfaces and interfaces, Chem. Rev. 112 (2012) 5520–5551.